Mon. Not. R. Astron. Soc. **393,** 1141–1156 (2009) doi:10.1111/j.1365-2966.2008.14221.x

A five-wave Harten–Lax–van Leer Riemann solver for relativistic magnetohydrodynamics

A. Mignone,[1,2]★ M. Ugliano[2] and G. Bodo[1]

[1] *INAF/Osservatorio Astronomico di Torino, Strada Osservatorio 20, 10025 Pino Torinese, Italy*
[2] *Dipartimento di Fisica Generale 'Amedeo Avogadro', Università degli Studi di Torino, Via Pietro Giuria 1, 10125 Torino, Italy*

Accepted 2008 November 7. Received 2008 October 17; in original form 2008 August 28

ABSTRACT

We present a five-wave Riemann solver for the equations of ideal relativistic magnetohydrodynamics. Our solver can be regarded as a relativistic extension of the five-wave HLLD Riemann solver initially developed by Miyoshi & Kusano for the equations of ideal magnetohydrodynamics. The solution to the Riemann problem is approximated by a five-wave pattern, comprising two outermost fast shocks, two rotational discontinuities and a contact surface in the middle. The proposed scheme is considerably more elaborate than in the classical case since the normal velocity is no longer constant across the rotational modes. Still, proper closure to the Rankine–Hugoniot jump conditions can be attained by solving a non-linear scalar equation in the total pressure variable which, for the chosen configuration, has to be constant over the whole Riemann fan. The accuracy of the new Riemann solver is validated against one-dimensional tests and multidimensional applications. It is shown that our new solver considerably improves over the popular Harten–Lax–van Leer solver or the recently proposed HLLC schemes.

Key words: hydrodynamics – MHD – relativity – shock waves – methods: numerical.

1 MOTIVATIONS

Relativistic flows are involved in many of the high-energy astrophysical phenomena, such as, for example, jets in extragalactic radio sources, accretion flows around compact objects, pulsar winds and γ-ray bursts. In many instances, the presence of a magnetic field is also an essential ingredient for explaining the physics of these objects and interpreting their observational appearance.

Theoretical understanding of relativistic phenomena is subdue to the solution of the relativistic magnetohydrodynamics (RMHD) equations which, owing to their high degree of non-linearity, can hardly be solved by analytical methods. For this reason, the modelling of such phenomena has prompted the search for efficient and accurate numerical formulations. In this respect, Godunov-type schemes (Toro 1997) have gained increasing popularity due to their ability and robustness in accurately describing the sharp flow discontinuities such as shocks or tangential waves.

One of the fundamental ingredients of such schemes is the exact or approximate solution to the Riemann problem, i.e. the decay between two constant states separated by a discontinuity. Unfortunately, the use of an exact Riemann solver (Giacomazzo & Rezzolla 2006) is prohibitive because of the huge computational cost related to the high degree of non-linearities present in the equations. Instead, approximate methods of solution are preferred.

★E-mail: mignone@ph.unito.it

Linearized solvers (Komissarov 1999; Balsara 2001; Koldoba, Kuznetsov & Ustyugova 2002) rely on the rather convoluted eigenvector decomposition of the underlying equations and may be prone to numerical pathologies leading to negative density or pressures inside the solution (Einfeldt et al. 1991).

Characteristic-free algorithms based on the Rusanov Lax–Friedrichs or the Harten–Lax–van Leer (HLL, Harten, Lax & van Leer 1983) formulations are sometime preferred due to their ease of implementation and positivity properties. Implementation of such algorithms can be found in the codes described by Gammie, McKinney & Tóth (2003); Leismann et al. (2005); Del Zanna et al. (2007); van der Holst, Keppens & Meliani (2008). Although simpler, the HLL scheme approximates only two out of the seven waves by collapsing the full structure of the Riemann fan into a single average state. These solvers, therefore, are not able to resolve intermediate waves such as Alfvén, contact and slow discontinuities.

Attempts to restore the middle contact (or entropy) wave (HLLC, initially devised for the Euler equations by Toro, Spruce & Speares 1994) have been proposed by Mignone, Massaglia & Bodo (2005) in the case of purely transversal fields and by Mignone & Bodo (2006, hereafter MB) and Honkkila & Janhunen (2007) in the more general case. These schemes provide a relativistic extension of the work proposed by Gurski (2004) and Li (2005) for the classical magnetohydrodynamics (MHD) equations.

HLLC solvers for the equations of MHD and RMHD, however, still do not capture slow discontinuities and Alfvén waves. Besides, direct application of the HLLC solver of MB to genuinely

three-dimensional problems was shown to suffer from a (potential) pathological singularity when the component of magnetic field normal to a zone interface approaches zero.

A step forward in resolving intermediate wave structures was then performed by Miyoshi & Kusano (2005, hereafter MK) who, in the context of Newtonian MHD, introduced a four state solver (HLLD) restoring the rotational (Alfvén) discontinuities. In this paper, we propose a generalization of Miyoshi & Kusano approach to the equations of relativistic MHD. As we will see, this task is greatly entangled by the different nature of relativistic rotational waves across which the velocity component normal to the interface is no longer constant. The proposed algorithm has been implemented in the PLUTO code for astrophysical fluid dynamics (Mignone et al. 2007) which embeds a computational infrastructure for the solution of different sets of equations (e.g. Euler, MHD or relativistic MHD conservation laws) in the finite volume formalism.

The paper is structured as follows: in Section 2, we briefly review the equations of RMHD and formulate the problem. In Section 3, the new Riemann solver is derived. Numerical tests and astrophysical applications are presented in Section 4 and conclusions are drawn in Section 5.

2 BASIC EQUATIONS

The equations of RMHD are derived under the physical assumptions of constant magnetic permeability and infinite conductivity, appropriate for a perfectly conducting fluid (Lichnerowicz 1967; Anile 1990). In divergence form, they express particle number and energy-momentum conservation:

$$\partial_\mu(\rho u^\mu) = 0, \tag{1}$$

$$\partial_\mu\left[\left(w_{\rm g}+b^2\right)u^\mu u^\nu - b^\mu b^\nu + \left(p_{\rm g}+\frac{b^2}{2}\right)\eta^{\mu\nu}\right] = 0, \tag{2}$$

$$\partial_\mu\left(u^\mu b^\nu - u^\nu b^\mu\right) = 0\,, \tag{3}$$

where ρ is the rest mass density, $u^\mu = \gamma(1, \boldsymbol{v})$ is the four velocity ($\gamma \equiv$ Lorentz factor, $\boldsymbol{v} \equiv$ three velocity), $w_{\rm g}$ and $p_{\rm g}$ are the gas enthalpy and thermal pressure, respectively, and $\eta^{\mu\nu}$ is the Minkowski metric tensor. The covariant magnetic field b^μ is orthogonal to the fluid four velocity ($u^\mu b_\mu = 0$) and related to the laboratory frame field $\boldsymbol{B}$ by

$$b^\mu = \left[\gamma\,\boldsymbol{v}\cdot\boldsymbol{B},\ \frac{\boldsymbol{B}}{\gamma} + \gamma\,(\boldsymbol{v}\cdot\boldsymbol{B})\,\boldsymbol{v}\right]. \tag{4}$$

In equation (2), $b^2 \equiv b^\mu b_\mu = \boldsymbol{B}^2/\gamma^2 + (\boldsymbol{v}\cdot\boldsymbol{B})^2$ is the squared magnitude of the magnetic field.

The set of equations (1)–(3) must be complemented by an equation of state which may be taken as the constant Γ law:

$$w_{\rm g} = \rho + \frac{\Gamma}{\Gamma-1}p_{\rm g}, \tag{5}$$

where Γ is the specific heat ratio. Alternative equations of state (see e.g. Mignone & McKinney 2007) may be adopted.

In the following, we will be dealing with the one-dimensional conservation law:

$$\frac{\partial \boldsymbol{U}}{\partial t} + \frac{\partial \boldsymbol{F}}{\partial x} = 0, \tag{6}$$

which follows directly from equations (1)–(3) by discarding contributions from y and z. Conserved variables and corresponding fluxes take the form

$$\boldsymbol{U} = \begin{pmatrix} D \\ m^k \\ E \\ B^k \end{pmatrix}, \quad \boldsymbol{F} = \begin{pmatrix} Dv^x \\ wu^x u^k - b^x b^k + p\delta_{kx} \\ m^x \\ B^k v^x - B^x v^k \end{pmatrix}, \tag{7}$$

where $k = x, y, z$, $D = \rho\gamma$ is the density as seen from the observer's frame while, introducing $w \equiv w_{\rm g} + b^2$ (total enthalpy) and $p \equiv p_{\rm g} + b^2/2$ (total pressure),

$$m^k = wu^0u^k - b^0b^k, \quad E = wu^0u^0 - b^0b^0 - p \tag{8}$$

are the momentum and energy densities, respectively. δ_{kx} is the Kronecker delta symbol.

Note that, since $F_{B^x} = 0$, the normal component of magnetic field (B^x) does not change during the evolution and can be regarded as a parameter. This is a direct consequence of the $\nabla\cdot\boldsymbol{B} = 0$ condition.

A conservative discretization of equation (6) over a time-step Δt yields

$$\boldsymbol{U}_i^{n+1} = \boldsymbol{U}_i^n - \frac{\Delta t}{\Delta x}\left(\boldsymbol{f}_{i+\frac{1}{2}} - \boldsymbol{f}_{i-\frac{1}{2}}\right), \tag{9}$$

where Δx is the mesh spacing and $\boldsymbol{f}_{i+\frac{1}{2}}$ is the upwind numerical flux computed at zone faces $x_{i+\frac{1}{2}}$ by solving, for $t^n < t < t^{n+1}$, the initial value problem defined by equation (6) together with the initial condition:

$$\boldsymbol{U}(x, t^n) = \begin{cases} \boldsymbol{U}_L & \text{for} \quad x < x_{i+\frac{1}{2}}, \\ \boldsymbol{U}_R & \text{for} \quad x > x_{i+\frac{1}{2}}, \end{cases} \tag{10}$$

where $\boldsymbol{U}_L$ and $\boldsymbol{U}_R$ are discontinuous left and right constant states on either side of the interface. This is also known as the Riemann problem. For a first order scheme, $\boldsymbol{U}_L = \boldsymbol{U}_i$ and $\boldsymbol{U}_R = \boldsymbol{U}_{i+1}$.

The decay of the initial discontinuity given by equation (10) leads to the formation of a self-similar wave pattern in the x–t plane, where fast, slow, Alfvén and contact modes can develop. At the double end of the Riemann fan, two fast magnetosonic waves bound the emerging pattern enclosing two rotational (Alfvén) discontinuities, two slow magnetosonic waves and a contact surface in the middle. The same patterns are also found in classical MHD. Fast and slow magnetosonic disturbances can be either shocks or rarefaction waves, depending on the pressure jump and the norm of the magnetic field. All variables (i.e. density, velocity, magnetic field and pressure) change discontinuously across a fast or a slow shock, whereas thermodynamic quantities such as thermal pressure and rest density remain continuous when crossing a relativistic Alfvén wave. Contrary to its classical counterpart, however, the tangential components of magnetic field trace ellipses instead of circles and the normal component of the velocity is no longer continuous across a rotational discontinuity, Komissarov (1997). Finally, through the contact mode, only density exhibits a jump while thermal pressure, velocity and magnetic field remain continuous.

The complete analytical solution to the Riemann problem in RMHD has been recently derived in closed form by Giacomazzo & Rezzolla (2006) and a number of properties regarding simple waves are also well established, see Anile & Pennisi (1987) and Anile (1990).

For the special case in which the component of the magnetic field normal to a zone interface vanishes, a degeneracy occurs where tangential, Alfvén and slow waves all propagate at the speed of the

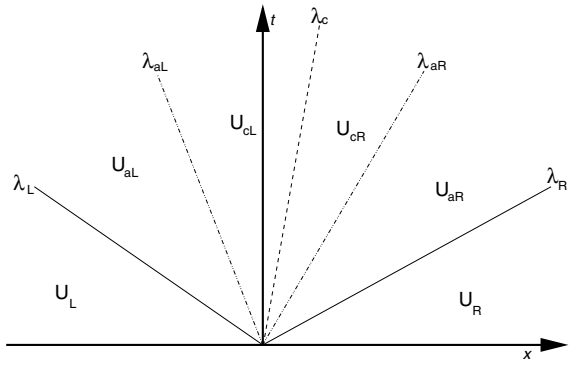

Figure 1. Approximate structure of the Riemann fan introduced by the HLLD solver. The initial states $\boldsymbol{U}_L$ and $\boldsymbol{U}_R$ are connected to each other through a set of five waves representing, clockwise, a fast shock λ_L, an rotational discontinuity λ_{aL}, a contact wave λ_c, an rotational discontinuity λ_{aR} and a fast shock λ_R. The outermost states, $\boldsymbol{U}_L$ and $\boldsymbol{U}_R$, are given as input to the problem, whereas the others must be determined consistently solving the Rankine–Hugoniot jump conditions.

fluid and the solution simplifies to a three-wave pattern, see Romero et al. (2005).

The high degree of non-linearity inherent to the RMHD equations makes seeking for an exact solution prohibitive in terms of computational costs and efficiency. For these reasons, approximate methods of solution are preferred instead.

3 THE HLLD APPROXIMATE RIEMANN SOLVER

Without loss of generality, we place the initial discontinuity at $x = 0$ and set $t^n = 0$.

Following MK, we make the assumption that the Riemann fan can be divided by five waves: two outermost fast shocks, λ_R and λ_L, enclosing two rotational discontinuities, λ_{aL} and λ_{aR}, separated by the entropy (or contact) mode with speed λ_c. Note that slow modes are not considered in the solution. The five waves divide the x–t plane into the six regions shown in Fig. 1, corresponding (from left- to right-hand panel) to the six states $\boldsymbol{U}_\alpha$ with $\alpha = L, aL, cL, cR, aR, R$.

The outermost states ($\boldsymbol{U}_L$ and $\boldsymbol{U}_R$) are given as inputs to the problem, while the remaining ones have to be determined. In the typical approach used to construct HLL-based solvers, the outermost velocities λ_L and λ_R are also provided as estimates from the input left and right states. As in MB, we choose to use the simple Davis estimate (Davis 1988).

Across any given wave λ, states and fluxes must satisfy the jump conditions

$$[\lambda \boldsymbol{U} - \boldsymbol{F}]_\lambda \equiv (\lambda \boldsymbol{U} - \boldsymbol{F})_+ - (\lambda \boldsymbol{U} - \boldsymbol{F})_- = 0, \tag{11}$$

where $+$ and $-$ identify, respectively, the state immediately ahead or behind the wave front. Note that for consistency with the integral form of the conservation law over the rectangle $[\lambda_L \Delta t, \lambda_R \Delta t] \times [0, \Delta t]$, one has, in general, $\boldsymbol{F}_\alpha \neq \boldsymbol{F}(\boldsymbol{U}_\alpha)$, except of course for $\alpha = L$ or $\alpha = R$.

Across the fast waves, we will make frequent use of

$$\boldsymbol{R}_L = \lambda_L \boldsymbol{U}_L - \boldsymbol{F}_L, \quad \boldsymbol{R}_R = \lambda_R \boldsymbol{U}_R - \boldsymbol{F}_R, \tag{12}$$

which are known vectors readily obtained from the left and right input states. A particular component of $\boldsymbol{R}$ is selected by mean of a subscript, e.g. R_D is the density component of $\boldsymbol{R}$.

A consistent solution to the problem has to satisfy the seven non-linear relations implied by equation (11) for each of the five waves considered, thus giving a total of 35 equations. Moreover, physically relevant solutions must fulfill a number of requirements in order to reflect the characteristic nature of the considered waves. For this reason, across the contact mode, we demand that velocity, magnetic field and total pressure be continuous:

$$[\boldsymbol{v}]_{\lambda_c} = [\boldsymbol{B}]_{\lambda_c} = \boldsymbol{0}, \quad [p]_{\lambda_c} = 0, \tag{13}$$

and require that $\lambda_c \equiv v_c^x$, i.e. the contact wave moves at the speed of the fluid. However, density, energy and total enthalpy may be discontinuous. On the other hand, through the rotational waves λ_{aL} and λ_{aR}, scalar quantities such as total pressure and enthalpy are invariant whereas all vector components (except for B^x) experience jumps.

Since slow magnetosonic waves are not considered, we naturally conclude that only the total pressure remains constant throughout the fan, contrary to Newtonian MHD, where also the velocity normal to the interface (v^x) is left unchanged across the waves. This is an obvious consequence of the different nature of relativistic Alfvén waves across which vector fields like u^μ and b^μ trace ellipses rather than circles. As a consequence, the normal component of the velocity, v^x, is no longer invariant in RMHD but experiences a jump. These considerations along with the higher level of complexity of the relativistic equations make the extension of the multistate HLL solver to RMHD considerably more elaborate.

Our strategy of solution is briefly summarized. For each state, we introduce a set of eight *independent* unknowns: $\mathcal{P} = \{D, v^x, v^y, v^z, B^y, B^z, w, p\}$ and write conservative variables and fluxes given by equation (7) as

$$\boldsymbol{U}_\alpha = \begin{pmatrix} D \\ w\gamma^2 v^k - b^0 b^k \\ w\gamma^2 - p - b^0 b^0 \\ B^k \end{pmatrix}_\alpha, \tag{14}$$

$$\boldsymbol{F}_\alpha = \begin{pmatrix} Dv^x \\ w\gamma^2 v^k v^x - b^k b^x + p\delta_{kx} \\ w\gamma^2 v^x - b^0 b^x \\ B^k v^x - B^x v^k \end{pmatrix}_\alpha, \tag{15}$$

where $k = x, y, z$ labels the vector component, α is the state and b^μ is computed directly from equation (4). We proceed by solving, as function of the total pressure p, the jump conditions (equation 11) across the outermost waves λ_L and λ_R. By requiring that total pressure and Alfvén velocity do not change across each rotational modes, we find a set of invariant quantities across λ_{aL} and λ_{aR}. Using these invariants, we express states and fluxes on either side of the contact mode ($\alpha = cL, cR$) in terms of the total pressure unknown only. Imposing continuity of normal velocity, $v_{cL}^x(p) = v_{cR}^x(p)$, leads to a non-linear scalar equation in p, whose zero gives the desired solution.

Once p has been found to some relative accuracy (typically 10^{-6}), the full solution to the problem can be written as

$$\boldsymbol{f} = \begin{cases} \boldsymbol{F}_L & \text{if} \quad \lambda_L > 0 \\ \boldsymbol{F}_{aL} & \text{if} \quad \lambda_L < 0 < \lambda_{aL} \\ \boldsymbol{F}_{aL} + \lambda_{\rm c}\,(\boldsymbol{U}_{cL} - \boldsymbol{U}_{aL}) & \text{if} \quad \lambda_{aL} < 0 < \lambda_{\rm c} \\ \boldsymbol{F}_{aR} + \lambda_{\rm c}\,(\boldsymbol{U}_{cR} - \boldsymbol{U}_{aR}) & \text{if} \quad \lambda_{\rm c} < 0 < \lambda_{aR} \\ \boldsymbol{F}_{aR} & \text{if} \quad \lambda_{aR} < 0 < \lambda_R \\ \boldsymbol{F}_R & \text{if} \quad \lambda_R < 0 \end{cases} \tag{16}$$

where $\boldsymbol{U}_{aL}$, $\boldsymbol{U}_{aR}$ are computed in Section 3.1, $\boldsymbol{U}_{cL}$, $\boldsymbol{U}_{cR}$ in Section 3.3 and $\boldsymbol{F}_a = \boldsymbol{F} + \lambda_a(\boldsymbol{U}_a - \boldsymbol{U})$ (for $a = aL$ or $a = aR$) follow from the jump conditions. The wave speeds λ_{aL}, λ_{aR} and $\lambda_{\rm c}$ are computed during the solution process.

Here and in what follows, we adopt the convention that single subscripts like a (or c) refer indifferently to aL, aR (or cL, cR). Thus, an expression like $w_{\rm c} = w_a$ means $w_{cL} = w_{aL}$ and $w_{cR} = w_{aR}$.

3.1 Jump conditions across the fast waves

We start by explicitly writing the jump conditions across the outermost fast waves:

$$(\lambda - v^x)\, D = R_D, \tag{17}$$

$$(\lambda - v^x)\, w\gamma^2 v^k + b^k \left(b^x - \lambda b^0\right) - p\delta_{kx} = R_{{\rm m}^k}, \tag{18}$$

$$(\lambda - v^x) w\gamma^2 - \lambda p + b^0 \left(b^x - \lambda b^0\right) = R_E, \tag{19}$$

$$(\lambda - v^x)\, B^k + B^x v^k = R_{B^k}, \tag{20}$$

where, to avoid cluttered notations, we omit in this section the $\alpha = aL$ (when $\lambda = \lambda_L$) or $\alpha = aR$ (when $\lambda = \lambda_R$) index from the quantities appearing on the left-hand side. Similarly, the R's appearing on the right-hand sides of equations (17)–(20) are understood as the components of the vector $\boldsymbol{R}_L$ (when $\lambda = \lambda_L$) or $\boldsymbol{R}_R$ (when $\lambda = \lambda_R$), defined by equation (12).

The jump conditions of Faraday's law allow us to express the magnetic field as a function of velocities alone:

$$B^k = \frac{R_{B^k} - B^x v^k}{\lambda - v^x} \qquad \text{for} \qquad k = y, z. \tag{21}$$

The energy and momentum equations can be combined together to provide an explicit functional relation between the three components of velocity and the total pressure p. To this purpose, we first multiply the energy equation (19) times v^k and then subtract the resulting expression from the jump condition for the kth component of momentum, equation (18). Using equation (20) to get rid of the $\boldsymbol{v}^2$ term, one finds after some algebra

$$B^k\,(B^x - \boldsymbol{R}_B \cdot \boldsymbol{v}) - p\left(\delta_{kx} - \lambda v^k\right) = R_{{\rm m}^k} - v^k R_E, \tag{22}$$

with B^k defined by equation (21). The system can be solved for v^k giving

$$v^x = \frac{B^x\,(AB^x + \lambda C) - (A + G)\,(p + R_{{\rm m}^x})}{X}, \tag{23}$$

$$v^y = \frac{Q R_{{\rm m}^y} + R_{B^y}\,[C + B^x\,(\lambda R_{{\rm m}^x} - R_E)]}{X}, \tag{24}$$

$$v^z = \frac{Q R_{{\rm m}^z} + R_{B^z}\,[C + B^x\,(\lambda R_{{\rm m}^x} - R_E)]}{X}, \tag{25}$$

where

$$A = R_{{\rm m}^x} - \lambda R_E + p(1 - \lambda^2), \tag{26}$$

$$G = R_{B^y} R_{B^y} + R_{B^z} R_{B^z}, \tag{27}$$

$$C = R_{{\rm m}^y} R_{B^y} + R_{{\rm m}^z} R_{B^z}, \tag{28}$$

$$Q = -A - G + (B^x)^2(1 - \lambda^2) \tag{29}$$

$$X = B^x(A\lambda B^x + C) - (A + G)(\lambda p + R_E). \tag{30}$$

Once the velocity components are expressed as functions of p, the magnetic field is readily found from equation (21), while the total enthalpy can be found using its definition, $w = (E + p)/\gamma^2 + (\boldsymbol{v}\cdot\boldsymbol{B})^2$, or by subtracting R_E from the inner product $\boldsymbol{v}^k \cdot \boldsymbol{R}_{\rm m}$, giving

$$w = p + \frac{R_E - \boldsymbol{v}\cdot\boldsymbol{R}_{\rm m}}{\lambda - v^x}, \tag{31}$$

where $\boldsymbol{R}_{\rm m} \equiv (R_{{\rm m}^x}, R_{{\rm m}^y}, R_{{\rm m}^z})$. Although equivalent, we choose to use this second expression. Since the v^k are functions of p alone, the total enthalpy w is also a function of the total pressure.

The remaining conserved quantities in the $\alpha = aL$ or $\alpha = aR$ regions can be computed once p has been found

$$D = \frac{R_D}{\lambda - v^x}, \tag{32}$$

$$E = \frac{R_E + pv^x - (\boldsymbol{v}\cdot\boldsymbol{B})\,B^x}{\lambda - v^x}, \tag{33}$$

$$m^k = (E + p)\,v^k - (\boldsymbol{v}\cdot\boldsymbol{B})\,B^k. \tag{34}$$

One can verify by direct substitution that the previous equations together with the corresponding fluxes, equation (15), satisfy the jump conditions given by equations (17)–(20).

3.2 Jump conditions across the Alfvén waves

Across the rotational waves, one could, in principle, proceed as for the outer waves, i.e. by explicitly writing the jump conditions. However, as we will see, the treatment greatly simplifies if one introduces the four vector:

$$\sigma^\mu = \eta u^\mu + b^\mu, \qquad \text{with} \qquad \eta = \pm\text{sign}(B^x)\sqrt{w}, \tag{35}$$

where, for reasons that will be clear later, we take the plus (minus) sign for the right (left) state. From σ^μ, we define the spatial vector $\boldsymbol{K} \equiv (K^x, K^y, K^z)$ with components given by

$$K^k \equiv \frac{\sigma^k}{\sigma^0} = v^k + \frac{B^k}{\gamma\sigma^0}. \tag{36}$$

The vector $\boldsymbol{K}$ has some attractive properties, the most remarkable of which is that the x component coincides with the propagation speed of the Alfvén wave (Anile 1990). For this reason, we are motivated to define $\lambda_a \equiv K^x_a$, where the subscript a stands for either the left or right rotational wave (i.e. aL or aR) since we require that both K^x and p are invariant across the rotational discontinuity, i.e. $K^x_{\rm c} - K^x_a = p_{\rm c} - p_a = 0$, a property certainly shared by the exact solution. As we will show, this choice naturally reduces to the expressions found by MK in the non-relativistic limit.

Indeed, setting $\lambda_a = K^x_a = K^x{}_{\rm c}$ and using equation (36) to express v^k as functions of K^k, the jump conditions simplify to

$$\left[\frac{DB^x}{\gamma\sigma^0}\right]_{\lambda_a} = 0 \tag{37}$$

$$\left[\frac{\eta\sigma^k B^x}{\sigma^0} - p\delta_{kx}\right]_{\lambda_a} = 0 \tag{38}$$

$$\left[\eta B^x - \frac{\sigma^x}{\sigma^0}p\right]_{\lambda_a} = 0 \tag{39}$$

$$\left[\frac{B^x\sigma^k}{\sigma^0}\right]_{\lambda_a} = 0. \tag{40}$$

Since also $[p]_{\lambda_a} = 0$, the previous equations further also imply that (when $B^x \neq 0$) $D/(\gamma\sigma^0)$, w, K^y and K^z do not change across λ_a:

$$\boldsymbol{K}_{aL} = \boldsymbol{K}_{cL} \equiv \boldsymbol{K}_L, \quad \eta_{aL} = \eta_{cL} = \eta_L \tag{41}$$

$$\boldsymbol{K}_{aR} = \boldsymbol{K}_{cR} \equiv \boldsymbol{K}_R, \quad \eta_{aR} = \eta_{cR} = \eta_R \tag{42}$$

Being invariant, $\boldsymbol{K}$ can be computed from the state lying to the left (for λ_{aL}) or right (for λ_{aR}) of the discontinuity, thus being a function of the total pressure p alone. Instead of using equation (36), an alternative and more convenient expression may be found by properly replacing v^k with K^k in equations (17)–(20). After some algebra, one finds the simpler expression

$$K^k = \frac{R_{\rm m}{}^k + p\delta_{kx} + R_{B^k}\eta}{\lambda p + R_E + B^x\eta}, \tag{43}$$

still being a function of the total pressure p.

Note that, similarly to its non-relativistic limit, we cannot use the relations in equations (37)–(40) to compute the solution across the rotational waves, since they do not provide enough independent relations. Instead, a solution may be found by considering the jump conditions across both rotational discontinuities and properly matching them using the conditions at the contact mode.

3.3 Jump conditions across the contact wave

At the contact discontinuity (CD) only density and total enthalpy can be discontinuous, while total pressure, normal and tangential fields are continuous as expressed by equation (13).

Since the magnetic field is a conserved quantity, one can immediately use the consistency condition between the innermost waves λ_{aL} and λ_{aR} to find B^k across the CD. Indeed, from

$$\begin{aligned}(\lambda_{\rm c} - \lambda_{aL})\,\boldsymbol{U}_{cL} + (\lambda_{aR} - \lambda_{\rm c})\,\boldsymbol{U}_{cR} = \\ = \lambda_{aR}\boldsymbol{U}_{aR} - \lambda_{aL}\boldsymbol{U}_{aL} - \boldsymbol{F}_{aR} + \boldsymbol{F}_{aL},\end{aligned} \tag{44}$$

one has $B^k_{cL} = B^k_{cR} \equiv B^k_{\rm c}$, where

$$B^k_{\rm c} = \frac{\left[B^k(\lambda - v^x) + B^x v^k\right]_{aR} - \left[B^k(\lambda - v^x) + B^x v^k\right]_{aL}}{\lambda_{aR} - \lambda_{aL}}. \tag{45}$$

Since quantities in the aL and aR regions are given in terms of the p unknown, equation (45) is also functions of p alone.

At this point, we take advantage of the fact that $\sigma^\mu u_\mu = -\eta$ to replace $\gamma\sigma^0$ with $\eta/(1 - \boldsymbol{K}\cdot\boldsymbol{v})$ and then rewrite equation (36) as

$$K^k = v^k + \frac{B^k}{\eta}(1 - \boldsymbol{K}\cdot\boldsymbol{v}) \qquad \text{for} \qquad k = x, y, z. \tag{46}$$

The previous equations form a linear system in the velocity components v^k and can be easily inverted to the left- and right-hand side of the CD to yield

$$v^k = K^k - \frac{B^k(1 - \boldsymbol{K}^2)}{\eta - \boldsymbol{K}\cdot\boldsymbol{B}} \qquad \text{for} \qquad k = x, y, z \tag{47}$$

which depend also on the total pressure variable only, with w and K^k being given by equations (31) and (43), and the $B^k_{\rm c}$s being computed from equation (45). Imposing continuity of the normal velocity across the CD, $v^x_{cL} - v^x_{cR} = 0$, results in

$$\Delta K^x\left[1 - B^x\,(Y_R - Y_L)\right] = 0, \tag{48}$$

where

$$Y_S(p) = \frac{1 - \boldsymbol{K}_S^2}{\eta_S\Delta K^x - \boldsymbol{K}_S\cdot\hat{\boldsymbol{B}}_{\rm c}}, \qquad S = L, R \tag{49}$$

is a function of p only, $\hat{\boldsymbol{B}}_{\rm c} \equiv \Delta K^x\boldsymbol{B}_{\rm c}$ is the numerator of equation (45) and $\Delta K^x = K^x_{aR} - K^x_{aL}$. Equation (48) is a non-linear function in p and must be solved numerically.

Once the iteration process has been completed and p has been found to some level of accuracy, the remaining conserved variables to the left- and right-hand sides of the CD are computed from the jump conditions across λ_{aL} and λ_{aR} and the definition of the flux, equation (15). Specifically one has, for $\{c = cL, a = aL\}$ or $\{c = cR, a = aR\}$,

$$D_{\rm c} = D_a\frac{\lambda_a - v^x_a}{\lambda_a - v^x_{\rm c}}, \tag{50}$$

$$E_{\rm c} = \frac{\lambda_a E_a - m^x_a + pv^x_{\rm c} - (\boldsymbol{v}_{\rm c}\cdot\boldsymbol{B}_{\rm c})\,B^x}{\lambda_a - v^x_{\rm c}}, \tag{51}$$

$$m^k_{\rm c} = (E_{\rm c} + p)v^k_{\rm c} - (\boldsymbol{v}_{\rm c}\cdot\boldsymbol{B}_{\rm c})\,B^k_{\rm c}. \tag{52}$$

This concludes the derivation of our Riemann solver.

3.4 Full solution

In the previous sections, we have shown that the whole set of jump conditions can be brought down to the solution of a single non-linear equation, given by equation (48), in the total pressure variable p. In the particular case of vanishing normal component of the magnetic field, i.e. $B_x \to 0$, this equation can be solved exactly as discussed in Section 3.4.1.

For the more general case, the solution has to be found numerically using an iterative method where, starting from an initial guess $p^{(0)}$, each iteration consists of the following steps.

(i) Given a new guess value $p^{(k)}$ to the total pressure, start from equation (23)–(25) to express $\boldsymbol{v}_{aL}$ and $\boldsymbol{v}_{aR}$ as functions of the total pressure. Also, express magnetic fields $\boldsymbol{B}_{aL}$, $\boldsymbol{B}_{aR}$ and total enthalpies w_L, w_R using equations (21) and (31), respectively.

(ii) Compute $\boldsymbol{K}_{aL}$ and $\boldsymbol{K}_{aR}$ using equation (43) and the transverse components of $\boldsymbol{B}_{\rm c}$ using equation (45).

(iii) Use equation (48) to find the next improved iteration value.

For the sake of assessing the validity of our new solver, we choose the secant method as our root-finding algorithm. The initial guess is provided using the following prescription:

$$p^{(0)} = \begin{cases} p_0 & \text{when} \quad (B^x)^2/p^{\rm hll} < 0.1, \\ p^{\rm hll} & \text{otherwise}, \end{cases} \tag{53}$$

where $p^{\rm hll}$ is the total pressure computed from the HLL average state whereas p_0 is the solution in the $B^x = 0$ limiting case. Extensive

numerical testing has shown that the total pressure $p^{\rm hll}$ computed from the HLL average state provides, in most cases, a sufficiently close guess to the correct physical solution, so that no more than five to six iterations (for zones with steep gradients) were required to achieve a relative accuracy of 10^{-6}.

The computational cost depends on the simulation setting since the average number of iterations can vary from one problem to another. However, based on the results presented in Section 4, we have found that HLLD was at most a factor of $\sim$2 slower than HLL.

For a solution to be physically consistent and well behaved, we demand that

$$\begin{cases} w_L > p, \quad v^x_{aL} > \lambda_L, \quad v^x_{cL} > \lambda_{aL}, \\ w_R > p, \quad v^x_{aR} < \lambda_R, \quad v^x_{cR} < \lambda_{aR}, \end{cases} \tag{54}$$

hold simultaneously. These conditions guarantee positivity of density and that the correct eigenvalue ordering is always respected. We warn the reader that equation (48) may have, in general, more than one solution and that the conditions given by equation (54) may actually prove helpful in selecting the correct one. However, the intrinsic non-linear complexity of the RMHD equations makes it rather arduous and challenging to prove, a priori, both the existence and the uniqueness of a physically relevant solution, in the sense provided by equation (54). On the contrary, we encountered sporadic situations where none of the zeroes of equation (48) is physically admissible. Fortunately, these situations turn out to be rare eventualities caused either by a large jump between left and right states (as at the beginning of integration) or by under or overestimating the propagation speeds of the outermost fast waves, λ_L and λ_R. The latter conclusion is supported by the fact that, enlarging one or both wave speeds, led to a perfectly smooth and unique solution.

Therefore, we propose a safety mechanism whereby we switch to the simpler HLL Riemann solver whenever at least one or more of the conditions in equation (54) is not fulfilled. From several numerical tests, including the ones shown here, we found that the occurrence of these anomalies to be limited to few zones of the computational domain, usually less than 0.1 per cent in the tests presented here.

We conclude this section by noting that other more sophisticated algorithms may, in principle, be sought. One could, for instance, provide a better guess to the outer wave speeds λ_L and λ_R or even modify them accordingly until a solution is guaranteed to exist. Another, perhaps more useful, possibility is to bracket the solution inside a closed interval $[p_{\rm min}, p_{\rm max}]$, where $p_{\rm min}$ and $p_{\rm max}$ may be found from the conditions (equation 54). Using an alternative root finder, such as Ridder (Press et al. 1992), guarantees that the solution never jumps outside the interval. However, due to the small number of failures usually encountered, we do not think these alternatives could lead to a significant gain in accuracy.

3.4.1 Zero normal field limit

In the limit $B^x \to 0$, a degeneracy occurs where the Alfvén (and slow) waves propagate at the speed of the contact mode which thus becomes a tangential discontinuity. Across this degenerate front, only normal velocity and total pressure remain continuous, whereas tangential vector fields are subject to jumps.

This case does not pose any serious difficulty in our derivation and can be solved exactly. Indeed, by setting $B^x = 0$ in equations (43) and (48), one immediately finds that $K^x_R = K^x_L = v^x_{\rm c}$ leading to the following quadratic equation for p:

$$p^2 + \left(E^{\rm hll} - F^{\rm hll}_{{\rm m}^x}\right) p + m^{x,{\rm hll}} F^{\rm hll}_E - F^{\rm hll}_{{\rm m}^x} E^{\rm hll} = 0, \tag{55}$$

where the superscript 'hll' refers to the HLL average state or flux given by equation (28) or (31) of MB. We note that equation (55) coincides with the derivation given by MB (see also Mignone et al. 2005) in the same degenerate case and the positive root gives the correct physical solution. The intermediate states, $\boldsymbol{U}_{cL}$ and $\boldsymbol{U}_{cR}$, lose their physical meaning as $B^x \to 0$ but they never enter the solution since, as $\lambda_{aL}, \lambda_{aR} \to \lambda_{\rm c}$, only $\boldsymbol{U}_{aL}$ and $\boldsymbol{U}_{aR}$ will have a non-zero finite width, see Fig. 1.

Given the initial guess, equation (53), our proposed approach does not have to deal separately with the $B^x \neq 0$ and $B^x = 0$ cases (as in MB and Honkkila & Janhunen 2007) and thus solves the issue raised by MB.

3.4.2 Newtonian limit

We now show that our derivation reduces to the HLLD Riemann solver found by MK under the appropriate non-relativistic limit. We begin by noting that, for $\boldsymbol{v}/c \to 0$, the velocity and induction four-vectors reduce to $u^\mu \to (1, v^k)$ and $b^\mu \to (0, B^k)$, respectively. Also note that $w_{\rm g}, w \to \rho$ in the non-relativistic limit, so that

$$K^k \to v^k + s\frac{B^k}{\sqrt{\rho}}, \tag{56}$$

and thus v^x cannot change across λ_a. Replacing equations (17) and (18) with their non-relativistic expressions and demanding $v^x_a = v^x_{\rm c}$ gives, in our notations, the following expressions:

$$v^x_a = \frac{R_{R,{\rm m}^x} - R_{L,{\rm m}^x}}{R_{R,D} - R_{L,D}}, \tag{57}$$

$$p = (B^x)^2 - \frac{R_{L,{\rm m}^x} R_{R_{R,D}} - R_{R,{\rm m}^x} R_{R_{L,D}}}{R_{R,D} - R_{L,D}}, \tag{58}$$

which can be shown to be identical to equations (38) and (41) of MK. With little algebra, one can also show that the remaining variables in the aL and aR regions reduce to the corresponding non-relativistic expressions of MK. Similarly, the jump across the rotational waves is solved exactly in the same fashion, i.e. by solving the integral conservation laws over the Riemann fan. For instance, equation (45) reduces to equations (61) and (62) of MK. These results should not be surprising since, our set of parameters to write conserved variables and fluxes is identical to the one used by MK. The only exception is the energy, which is actually written in terms of the total enthalpy.

4 NUMERICAL TESTS

We now evaluate, in Section 4.1, the accuracy of the proposed HLLD Riemann solver by means of selected one-dimensional shock tube problems. Applications of the solver to multidimensional problems of astrophysical relevance are presented in Section 4.2.

4.1 One-dimensional shock tubes

The initial condition is given by equation (10) with left and right states defined by the primitive variables listed in Table 1. The computational domain is chosen to be the interval [0, 1] and the discontinuity is placed at $x = 0.5$. The resolution N_x and final integration time can be found in the last two columns of Table 1. Unless otherwise stated, we employ the constant Γ-law with $\Gamma = 5/3$. The RMHD equations are solved using the first-order accurate scheme (equation 9) with a Courant–Friedrichs–Lewy (CFL) number of 0.8.

Table 1. Initial conditions for the test problems discussed in the text. The last two columns give, respectively, the final integration time and the number of computational zones used in the computation.

Test	State	ρ	p_g	v^x	v^y	v^z	B^x	B^y	B^z	Time	Zones
Contact Wave	L	10	1	0	0.7	0.2	5	1	0.5	1	40
	R	1	1	0	0.7	0.2	5	1	0.5		
Rotational Wave	L	1	1	0.4	−0.3	0.5	2.4	1	−1.6	1	40
	R	1	1	0.377347	−0.482389	0.424190	2.4	−0.1	−2.178213		
Shock Tube 1	L	1	1	0	0	0	0.5	1	0	0.4	400
	R	0.125	0.1	0	0	0	0.5	−1	0		
Shock Tube 2	L	1.08	0.95	0.4	0.3	0.2	2	0.3	0.3	0.55	800
	R	1	1	−0.45	−0.2	0.2	2	−0.7	0.5		
Shock Tube 3	L	1	0.1	0.999	0	0	10	7	7	0.4	400
	R	1	0.1	−0.999	0	0	10	−7	−7		
Shock Tube 4	L	1	5	0	0.3	0.4	1	6	2	0.5	800
	R	0.9	5.3	0	0	0	1	5	2		

Numerical results are compared to the HLLC Riemann solver of MB and the simpler HLL scheme and the accuracy is quantified by computing discrete errors in L-1 norm:

$$\epsilon_{\rm L1} = \sum_{i=1}^{i=N_x} \left| q_i^{\rm ref} - q_i \right| \Delta x_i , \tag{59}$$

where q_i is the first-order numerical solution (density or magnetic field), $q_i^{\rm ref}$ is the reference solution at x_i and Δx_i is the mesh spacing. For tests 1, 2, 4, we obtained a reference solution using the second-order scheme of MB on 3200 zones and adaptive mesh refinement with six levels of refinement (equivalent resolution 204 800 grid points). Grid adaptivity in one-dimension has been incorporated in the PLUTO code using a block-structured grid approach following Berger & Colella (1989). For test 3, we use the exact numerical solution available from Giacomazzo & Rezzolla (2006). Errors (in per cent) are shown in Fig. 11 (later).

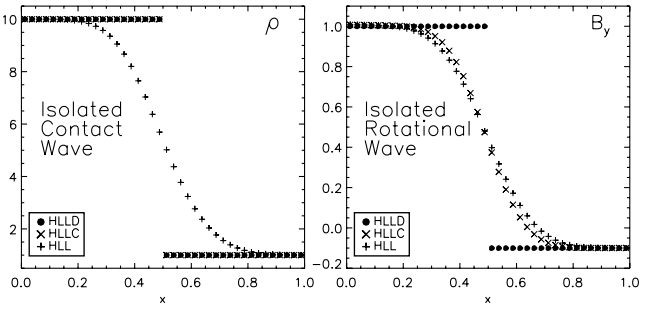

Figure 2. Results for the isolated contact (left-hand panel) and rotational (right-hand panel) waves at $t = 1$. Density and y component of magnetic field are shown, respectively. The different symbols show results computed with the new HLLD solver (filled circles), the HLLC solver (crosses) and the simpler HLL solver (plus signs). Note that only HLLD is able to capture exactly both discontinuities by keeping them perfectly sharp without producing any grid diffusion effect. HLLC can capture the contact wave but not the rotational discontinuity, whereas HLL spreads both of them on several grid zones.

4.1.1 Exact resolution of contact and Alfvén discontinuities

We now show that our HLLD solver can capture *exactly* isolated contact and rotational discontinuities. The initial conditions are listed at the beginning of Table 1.

In the case of an isolated stationary contact wave, only density is discontinuous across the interface. The left-hand panel in Fig. 2 shows the results at $t = 1$ computed with the HLLD, HLLC and HLL solvers: as expected, our HLLD produces no smearing of the discontinuity (as does HLLC). In contrast, the initial jump broadens over several grid zone when employing the HLL scheme.

Across a rotational discontinuity, scalar quantities such as proper density, pressure and total enthalpy are invariant but vector fields experience jumps. The left and right states on either side of an exact rotational discontinuity can be found using the procedure outlined in the appendix. The right-hand panel in Fig. 2 shows that only HLLD can successfully keep a sharp resolution of the discontinuity, whereas both HLLC and HLL spread the jump over several grid points because of the larger numerical viscosity.

4.1.2 Shock tube 1

The first shock tube test is a relativistic extension of the Brio Wu magnetic shock tube (Brio & Wu 1988) and has also been considered by Balsara (2001) and Del Zanna, Bucciantini & Londrillo (2003, hereafter dZBL) and in MB. The specific heat ratio is $\Gamma = 2$. The initial discontinuity breaks into a left-going fast rarefaction wave, a left-going compound wave, a contact discontinuity, a right-going slow shock and a right-going fast rarefaction wave. Rotational discontinuities are not generated.

In Figs 3 and 4, we plot the results obtained with the first-order scheme and compare them with the HLLC Riemann solver of MB and the HLL scheme. Although the resolution across the continuous right-going rarefaction wave is essentially the same, the HLLD solver offers a considerable improvement in accuracy in the structures located in the central region of the plots. Indeed, Fig. 4 shows an enlargement of the central part of the domain, where the compound wave (at $x \approx 0.51$), contact (at $x \approx 0.6$) and slow shock (at $x \approx 0.68$) are clearly visible. Besides the steeper profiles of the contact and slow modes, it is interesting to note that the compound wave, composed of a slow shock adjacent to a slow rarefaction wave, is notably better resolved with the HLLD scheme than with the other two.

These results are supported by the convergence study shown in the top left-hand panel of Fig. 11, demonstrating that the errors obtained with our new scheme are smaller than those obtained with the HLLC and HLL solvers (respectively). At the largest resolution employed, for example, the L-1 norm errors become ∼63 and

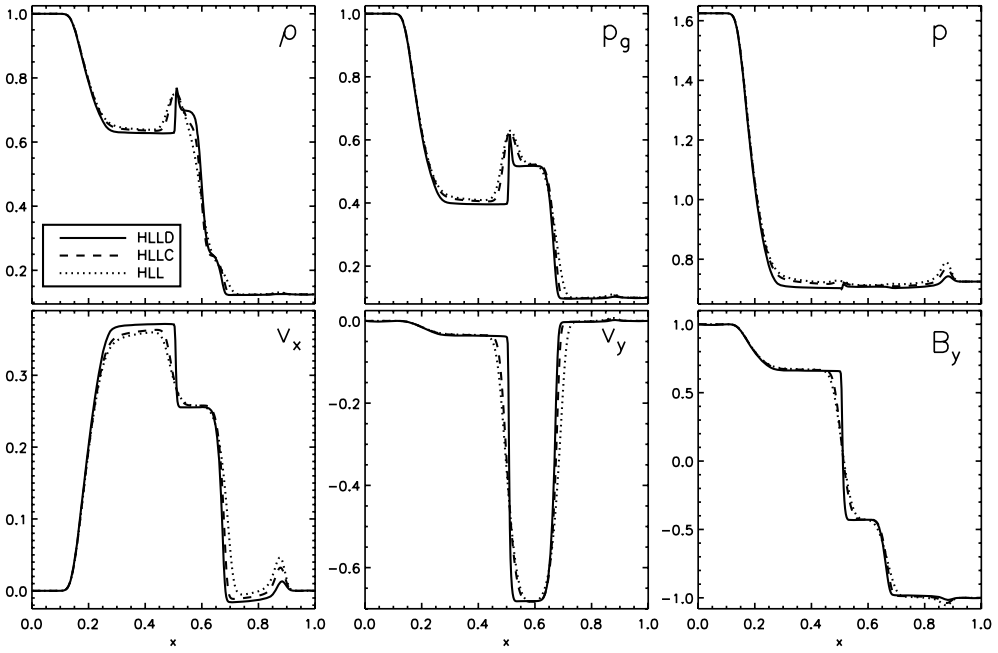

Figure 3. Relativistic Brio–Wu shock tube test at $t = 0.4$. Computations are carried on 400 zones using the HLLD (solid line), HLLC (dashed line) and HLL (dotted line) Riemann solver, respectively. The top panel shows, from left- to right-hand panel, the rest mass density, gas pressure and total pressure. The bottom panel shows the x and y components of velocity and the y component of magnetic field.

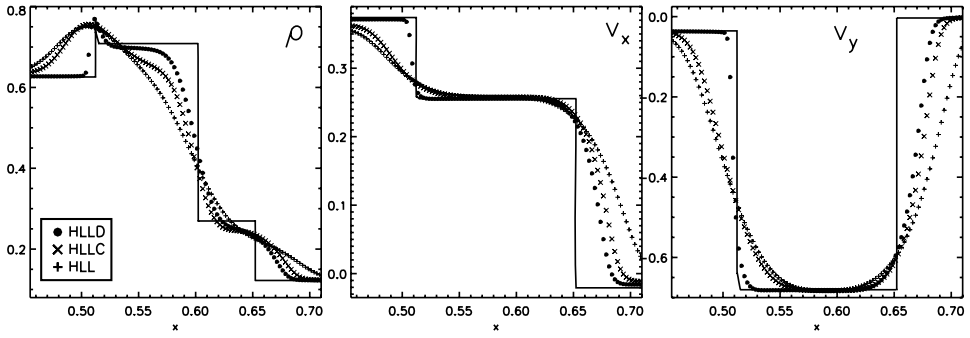

Figure 4. Enlargement of the central region of Fig. 3. Density and the two components of velocity are shown in the left-hand panel, central panel and right-hand panel, respectively. Diamonds, crosses and plus signs are used for the HLLD, HLLC and HLL Riemann solver, respectively. The reference solution is shown as a solid line.

∼49 per cent smaller than the HLL and HLLC schemes, respectively.

The CPU times required by the different Riemann solvers on this particular test were found to be scale as $t_{\rm hll} : t_{\rm hllc} : t_{\rm hlld} = 1{:}1.2{:}1.9$.

4.1.3 Shock tube 2

This test has also been considered in Balsara (2001) and MB, and the initial condition comes out as a non-planar Riemann problem implying that the change in orientation of the transverse magnetic field across the discontinuity is $\approx 0.55\pi$ (thus different from zero or π).

The emerging wave pattern consists of a contact wave (at $x \approx 0.475$) separating a left-going fast shock ($x \approx 0.13$), Alfvén wave ($x \approx 0.185$) and slow rarefaction ($x \approx 0.19$) from a slow shock ($x \approx 0.7$), Alfvén wave ($x \approx 0.725$) and fast shock ($x \approx 0.88$) heading to the right.

Computations carried out with the first-order accurate scheme are shown in Fig. 5 using the HLLD (solid line), HLLC (dashed line) and HLL (dotted line). The resolution across the outermost fast shocks is essentially the same for all Riemann solvers. Across the entropy mode, both HLLD and HLLC attain a sharper representation of the discontinuity albeit unphysical undershoots are visible immediately ahead of the contact mode. This is best noted in the left-hand panel of Fig. 6, where an enlargement of the same region is displayed.

On the right-hand side of the domain, the slow shock and the rotational wave propagate quite close to each other and the first-order scheme can barely distinguish them at a resolution of 800 zones. However, a close-up of the two waves (middle and right-hand panel in Fig. 6) shows that the proposed scheme is still more accurate than HLLC in resolving both fronts.

On the left-hand side, the separation between the Alfvén and slow rarefaction waves turns out to be even smaller and the two modes blur into a single wave because of the large numerical viscosity. This result is not surprising since these features are, in fact, challenging even for a second-order scheme (Balsara 2001).

Discrete L-1 errors computed using equation (59) are plotted as a function of the resolution in the top right-hand panel of Fig. 11. For this particular test, HLLD and HLLC produce comparable errors (∼1.22 and ∼1.33 per cent at the highest resolution) while HLL

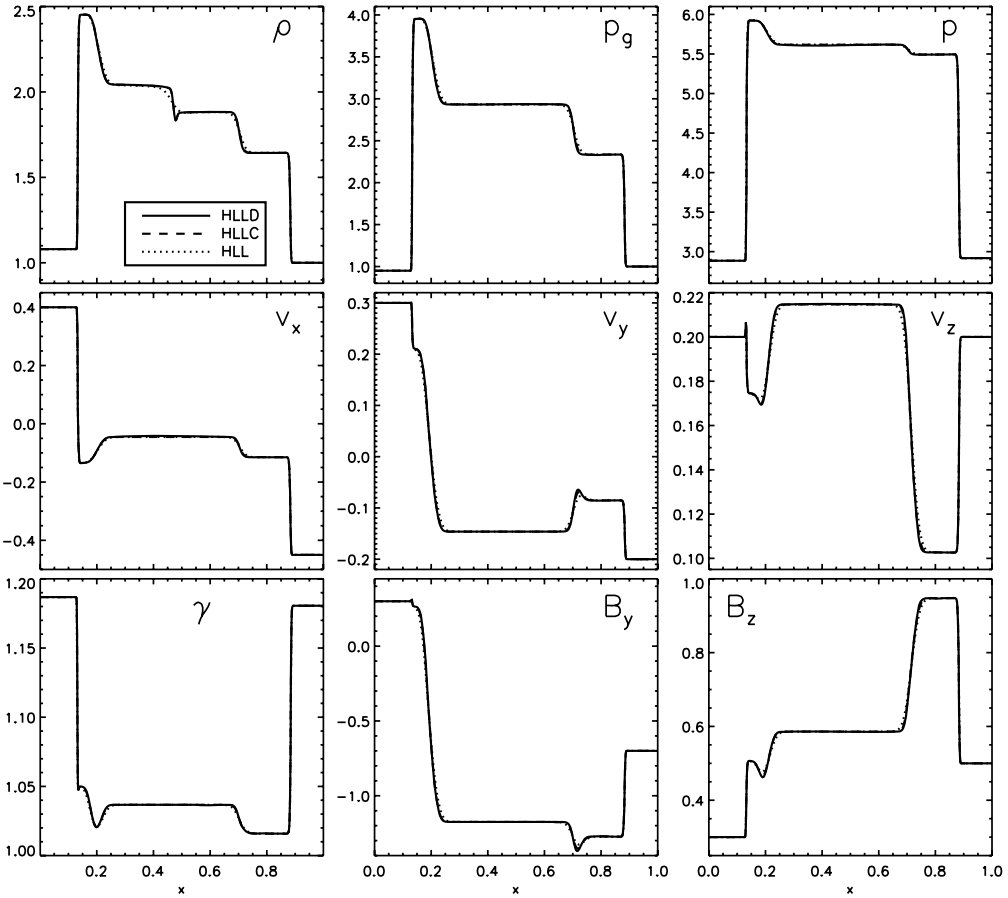

Figure 5. Results for the second shock tube problem at $t = 0.55$ on 800 grid points. From left- to right-hand panel, the top panel shows density, gas and total pressure. The middle panel shows the three components of velocity, whereas in the bottom panel we plot the Lorentz factor and the transverse components of magnetic field. Solid, dashed and dotted lines are used to identify results computed with HLLD, HLLC and HLL, respectively.

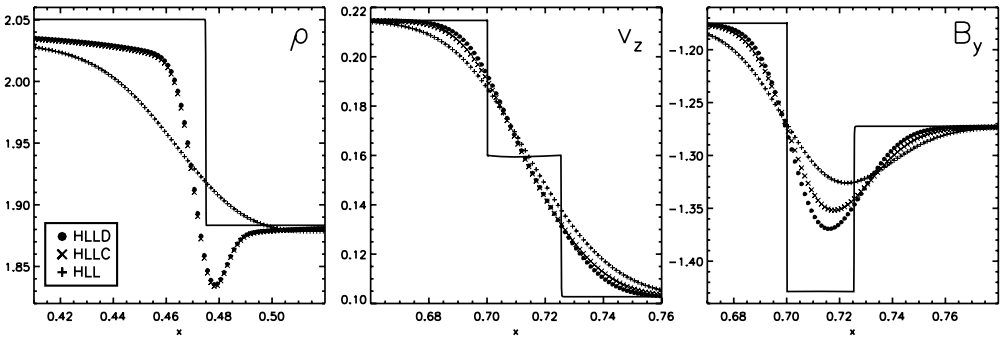

Figure 6. Left-hand panel: enlargement of the central region of Fig. 5 around the contact wave. Middle and right-hand panels: close-ups of the z component of velocity and y component of magnetic field around the right-going slow shock and Alfvén discontinuity. Different symbols refer to different Riemann solver, see the legend in the left-hand panel. The reference solution is shown as a solid line.

performs worse on contact, slow and Alfvén waves resulting in larger deviations from the reference solution.

The computational costs on 800 grid zones have found to be $t_{\rm hll} : t_{\rm hllc} : t_{\rm hlld} = 1{:}1.1{:}1.6$.

4.1.4 Shock tube 3

In this test problem, we consider the interaction of two oppositely colliding relativistic streams, see also Balsara (2001), dZBL and MB.

After the initial impact, two strong relativistic fast shocks propagate outwards symmetrically in opposite direction about the impact point, $x = 0.5$, see Fig. 7. Being a co-planar problem (i.e. the initial twist angle between magnetic fields is π), no rotational mode can actually appear. Two slow shocks delimiting a high-pressure constant density region in the centre follow behind.

Although no contact wave forms, the resolution across the slow shocks notably improves changing from HLL to HLLC and HLLC to HLLD, see Fig. 7 or the enlargement of the central region shown in

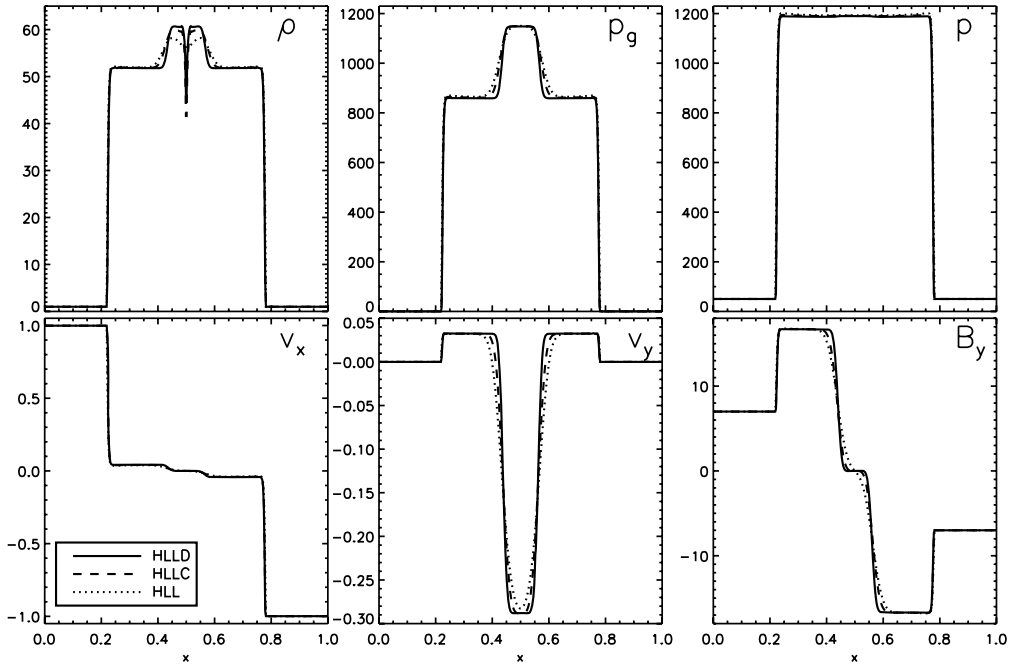

Figure 7. Relativistic collision of two oppositely moving streams at $t = 0.4$. From top to bottom, left to right, the panels show density ρ, gas pressure $p_{\rm g}$, total pressure p, x and y components of velocity ($v^x v^y$) and y component of magnetic field B^y. The z components have been omitted since they are identical to the y components. Solid, dashed and dotted lines refer to computations obtained with the HLLD, HLLC and HLL solvers. 400 computational zones were used in the computations.

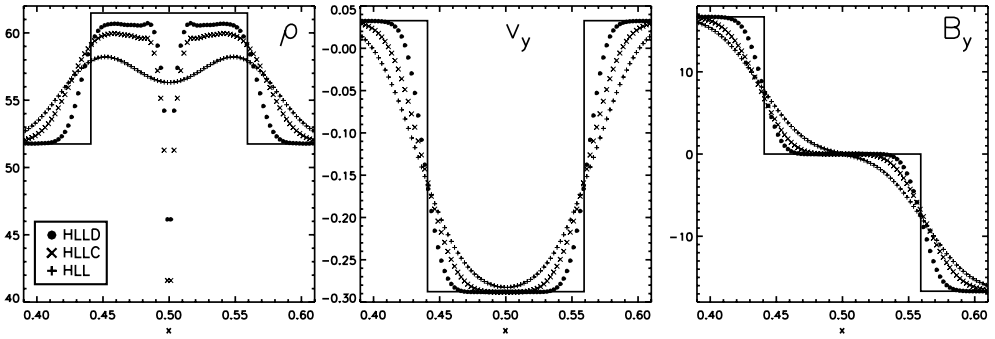

Figure 8. Enlargement of the central region in Fig. 7. Filled circles, crosses and plus sign have the same meaning as in Fig. 6. Note the wall heating problem evident in the density profile (left-hand panel). Central and right-hand panels show the transverse field profiles. The reference solution is shown as a solid line. Clearly, the resolution of the slow shocks ($x \approx 0.5 \pm 0.07$) improves from HLL to HLLC and more from HLLC to HLLD.

Fig. 8. The resolution across the outermost fast shocks is essentially the same for all solvers.

The spurious density undershoot at the centre of the grid is a notorious numerical pathology, known as the wall heating problem, often encountered in Godunov-type schemes (Noh 1987; Gehmeyr, Cheng & Mihalas 1997). It consists of an undesired entropy buildup in a few zones around the point of symmetry. Our scheme is obviously no exception as can be inferred by inspecting Fig. 7. Surprisingly, we note that error HLLD performs slightly better than HLLC. The numerical undershoots in density, in fact, are found to be ∼24 per cent (HLLD) and ∼32 per cent (HLLC). The HLL solver is less prone to this pathology most likely because of the larger numerical diffusion, see the left-hand panel close-up of Fig. 8.

Errors (for B^y) are computed using the exact solution available from Giacomazzo & Rezzolla (2006) which is free from the pathology just discussed. As shown in the bottom left-hand panel of Fig. 11, HLLD performs as the best numerical scheme yielding, at the largest resolution employed (3200 zones), L-1 norm errors of ∼18 per cent to be compared to ∼32 and ∼46 per cent of HLLC and HLL, respectively.

The CPU times for the different solvers on this problem follow the proportion $t_{\rm hll} : t_{\rm hllc} : t_{\rm hlld} = 1{:}1.1{:}1.4$.

4.1.5 Shock tube 4

The fourth shock tube test is taken from the 'Generic Alfvén' test in Giacomazzo & Rezzolla (2006). The breaking of the initial discontinuous states leads to the formation of seven waves. To the left of the contact discontinuity, one has a fast rarefaction wave, followed by a rotational wave and a slow shock. Travelling to the right of the contact discontinuity, one can find a slow shock, an Alfvén wave and a fast shock.

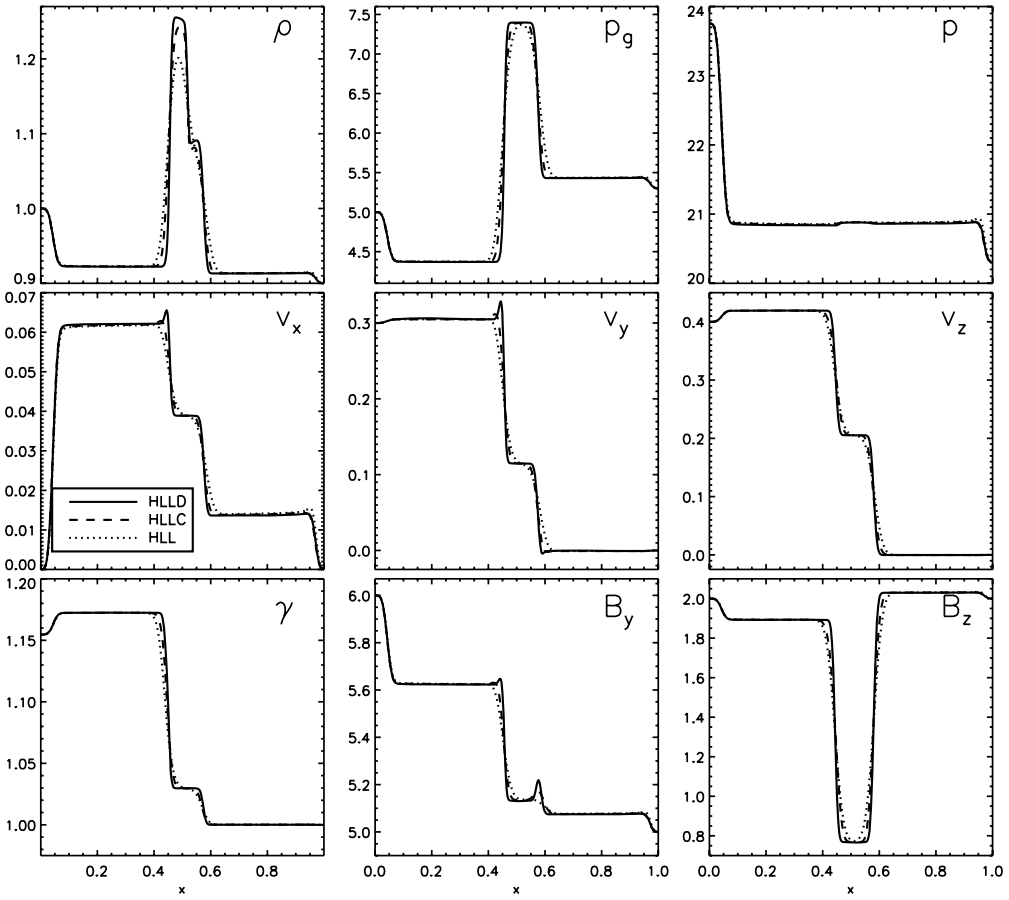

Figure 9. Results for the general Alfvén test, problem 4, at $t = 0.5$ on 800 computational zones. The panels are structured in a way similar to Fig. 5. Top panels: density, gas pressure and total pressure. Middle panels: x, y and z velocity components. Bottom panels: Lorentz factor γ and transverse components of magnetic field.

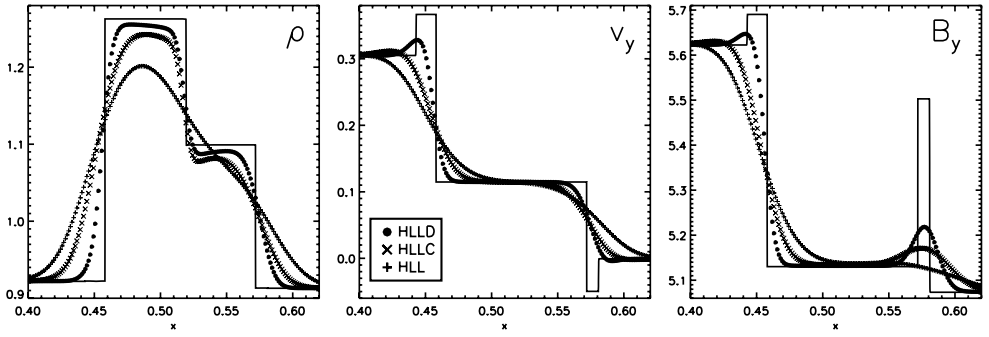

Figure 10. Magnification of the central region of Fig. 9. The left-hand panel shows the density profile where the two slow shocks and the central contact wave are clearly visible. Central and right-hand panels display the y components of velocity and magnetic field. The reference solution is shown as a solid line. Rotational modes can be most clearly distinguished only with the HLLD solver at $x \approx 0.44$ and 0.59.

We plot, in Fig. 9, the results computed with the HLLD, HLLC and HLL Riemann solvers at $t = 0.5$, when the outermost waves have almost left the outer boundaries. The central structure ($0.4 \lesssim x \lesssim 0.6$) is characterized by slowly moving fronts with the rotational discontinuities propagating very close to the slow shocks. At the resolution employed (800 zones), the rotational and slow modes appear to be visible and distinct only with the HLLD solver, whereas they become barely discernible with the HLLC solver and completely blend into a single wave using the HLL scheme. This is better shown in the enlargement of v^y and B^y profiles shown in Fig. 10: rotational modes are captured at $x \approx 0.44$ and 0.59 with the HLLD solver and gradually disappear when switching to the HLL scheme.

At the contact wave, HLLD and HLLC behave similarly but the sharper resolution attained at the left-going slow shock allows us to better capture the constant density shell between the two fronts.

Our scheme results in the smallest errors and numerical dissipation and exhibits a slightly faster convergence rate, see the plots in the bottom right-hand panel of Fig. 11. At low resolution, the errors obtained with HLL, HLLC and HLLD are in the ratio

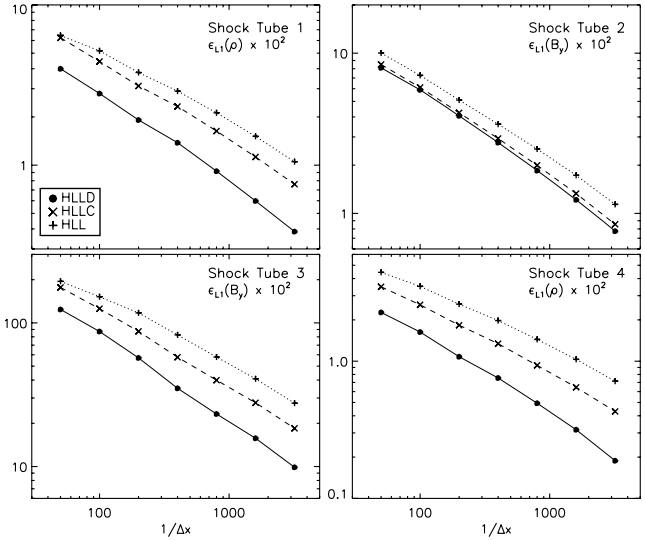

Figure 11. L-1 norm errors (in 10^2) for the four shock tube problems presented in the text as a function of the grid resolution. The different combinations of lines and symbols refer to HLLD (solid, circles), HLLC (dashed, crosses) and HLL (dotted, plus signs).

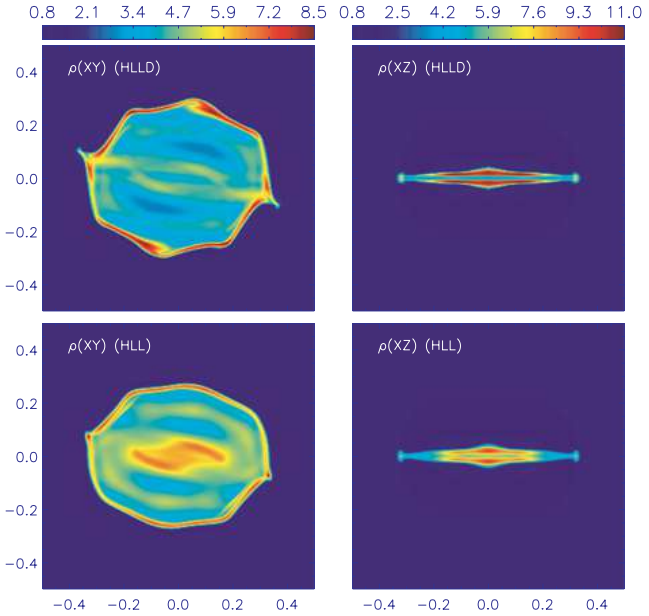

Figure 12. The three-dimensional rotor test problem computed with HLLD (top panels) and HLL (bottom panels) at the resolution of 256^3. Panels on the left-hand side show the density map (at $t = 0.4$) in the xy plane at $z = 0$ while panels to the right-hand side show the density in the xz plane at $y = 0$.

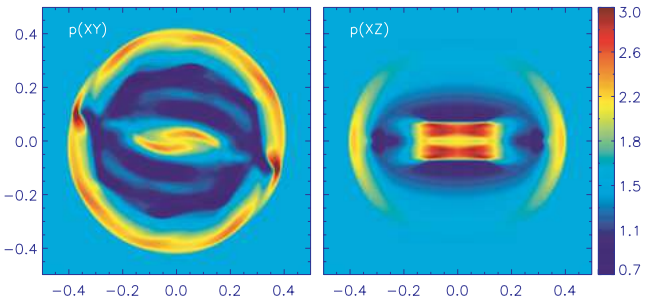

Figure 13. Same as Fig. 12 but showing the total pressure in the xy (left-hand panel) and xz (right-hand panel) panels for the HLLD solver.

1 : 0.75 : 0.45 while they become 1 : 0.6 : 0.27 as the mesh thickens. Correspondingly, the CPU running times for the three solvers at the resolution shown in Table 1 have found to scale as $t_{\rm hll} : t_{\rm hllc} : t_{\rm hlld} =$ 1:1.4:1.8. This example demonstrates the effectiveness and strength of adopting a more complete Riemann solver when describing the rich and complex features arising in relativistic magnetized flows.

4.2 Multidimensional tests

We have implemented our five-wave Riemann solver into the framework provided by the PLUTO code (Mignone et al. 2007). The constrained transport method is used to evolve the magnetic field. We use the third order, total variation diminishing Runge–Kutta scheme together with piecewise linear reconstruction.

4.2.1 The three-dimensional rotor problem

We consider a three-dimensional version of the standard rotor problem considered by dZBL. The initial condition consists of a sphere with radius $r_0 = 0.1$ centred at the origin of the domain taken to be the unit cube $[-1/2, 1/2]^3$. The sphere is heavier ($\rho = 10$) than the surrounding ($\rho = 1$) and rapidly spins around the z axis with velocity components given by $(v^x, v^y, v^z) = \omega(-y, x, 0)$, where $\omega = 9.95$ is the angular frequency of rotation. Pressure and magnetic field are constant everywhere, $p_{\rm g} = 1$, $\boldsymbol{B} = (1, 0, 0)$.

Exploiting the point symmetry, we carried computations until $t = 0.4$ at resolutions of 128^3, 256^3 and 512^3 using both the HLLD and HLL solvers. We point out that the HLLC of MB failed to pass this test, most likely because of the flux-singularity arising in three-dimensional computations in the zero normal field limit.

As the sphere starts rotating, torsional Alfvén waves propagate outward carrying angular momentum to the surrounding medium. The spherical structure gets squeezed into a disc configuration in the equatorial plane ($z = 0$) where the two collapsing poles collide generating reflected shocks propagating vertically in the upper and lower half-planes. This is shown in the four panels in Fig. 12 showing the density map in the xy and xz planes obtained with HLLD and HLL and in Fig. 13 showing the total pressure. After the impact, a hollow disc enclosed by a higher density shell at $z = \pm 0.02$ forms (top right-hand panels in Fig. 12). In the xy plane, matter is pushed in a thin, octagonal-like shell enclosed by a tangential discontinuity and what seems to be a slow rarefaction. The whole configuration is embedded in a spherical fast rarefaction front expanding almost radially. Flow distortions triggered by the discretization on a Cartesian grid are more pronounced with HLLD since we expect it to be more effective in the growth of small wavelength modes.

In Fig. 14, we compare the density profiles on the y and z axes for different resolutions and schemes. From both profiles, one can see that the central region tends to become more depleted as the resolution increases. Inspecting the profiles in the y direction (left-hand panel), we observe that HLL and HLLD tend to under and overestimate (respectively) the speed of the thin density shell when compared to the reference solution computed with the HLLD solver at a resolution of 512^3. The height of the shell peak is essentially the same for both solvers, regardless of the resolution.

In contrast, the right-hand panel of Fig. 14 shows a similar comparison along the vertical z axis. At the same resolution, HLL underestimates the density peak located at $z = 0.02$ and almost twice

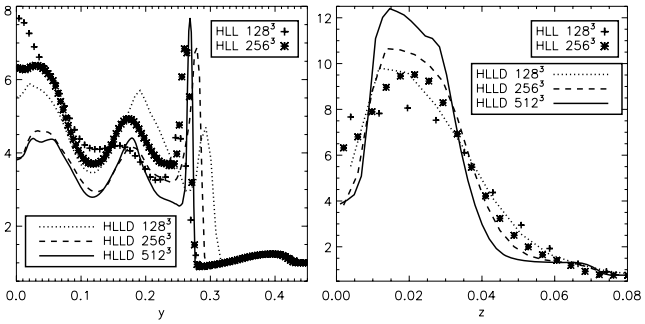

Figure 14. One-dimensional cuts along the y (left-hand panel) and z (right-hand panel) axes showing the density profiles at different resolutions ($128^3, 256^3$ and 512^3) and with different solvers. Solid, dashed and dotted lines are used for the HLLD solver whereas plus and star symbols are used for HLL.

the number of grid zones is needed to match the results obtained with the HLLD solver. The location of the front is approximately the same regardless of the solver.

In terms of computational cost, integration carried with the HLLD solver took approximately 1.6 that of HLL. This has to be compared with the CPU time required by HLL to reach a comparable level of accuracy which, doubling the resolution, would result in a computation $\sim 2^4$ as long. In this respect, three dimensional problems like the one considered here may prove specially helpful in establishing the trade-off between numerical efficiency and accuracy which, among other things, demand choosing between accurate (but expensive) solvers versus more diffusive (cheap) schemes.

4.2.2 *Kelvin–Helmholtz unstable flows*

The setup, taken from Bucciantini & Del Zanna (2006), consists of a two-dimensional planar Cartesian domain, $x \in [0, 1]$, $y \in [-1, 1]$ with a shear velocity profile given by

$$v^x = -\frac{1}{4}\tanh(100\, y). \tag{60}$$

Density and pressure are set constant everywhere and initialized to $\rho = 1, p_g = 20$, while magnetic field components are given in terms of the poloidal and toroidal magnetization parameters $\sigma_{\rm pol}$ and $\sigma_{\rm tor}$ as

$$(B^x, B^y, B^z) = \left(\sqrt{2\sigma_{\rm pol} p_g}, 0, \sqrt{2\sigma_{\rm tor} p_g}\right), \tag{61}$$

where we use $\sigma_{\rm pol} = 0.01, \sigma_{\rm tor} = 1$. The shear layer is perturbed by a non-zero component of the velocity:

$$v^y = \frac{1}{400}\sin(2\pi x)\exp\left[-\frac{y^2}{\beta^2}\right], \tag{62}$$

with $\beta = 1/10$, while we set $v^z = 0$. Computations are carried at low (L, 90×180 zones), medium (M, 180×360 zones) and high (H, 360×720 zones) resolution.

For $t \lesssim 5$, the perturbation follows a linear growth phase leading to the formation of a multiple vortex structure. In the high resolution (H) case, shown in Fig. 15, we observe the formation of a central vortex and two neighbours, more stretched ones. These elongated vortices are not seen in the computation of Bucciantini & Del Zanna (2006) who employed the HLL solver at our medium resolution. As expected, small-scale patterns are best spotted with the HLLD solver, while tend to be more diffused using the two-wave HLL scheme. The growth rate [computed as $\Delta v^y \equiv (v^y_{\rm max} - v^y_{\rm min})/2$, see top panel in Fig. 16] is closely related to the poloidal field amplification which, in turn, proceeds faster for smaller numerical resistivity (see the small subplot in the same panel) and thus for finer grids. Still, computations carried with the HLLD solver at low (L), medium (M) and high (H) resolutions reveal surprisingly similar growth rates and reach the saturation phase at essentially the same time ($t \approx 3.5$). In contrast, the saturation phase and the growth rate during the linear phase change with resolution when the HLL scheme is employed.

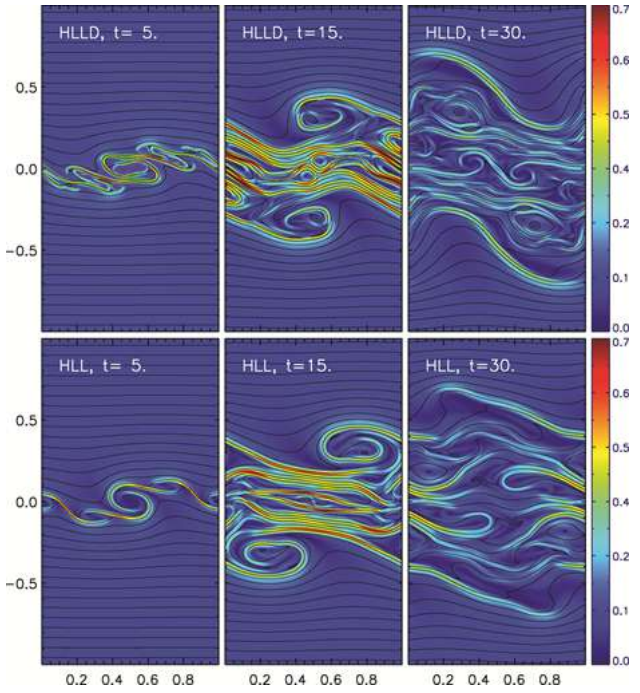

Figure 15. Colour scale maps of $\sqrt{B_x^2 + B_y^2}/B_z$ at different integration times, $t = 5$, 15, 30. Panels on top (bottom) refer to computations accomplished with HLLD (HLL). Poloidal magnetic field lines overlap.

Field amplification is prevented by reconnection events during which the field wounds up and becomes twisted by turbulent dynamics. Throughout the saturation phase (mid and right-hand panels in Fig. 15), the mixing layer enlarges and the field lines thicken into filamentary structures. Small-scale structure can be quantified by considering the power residing at large wavenumbers in the discrete Fourier transform of any flow quantity (we consider the y component of velocity). This is shown in the bottom panel of Fig. 16 where we plot the integrated power between $k_s/2$ and k_s as function of time (k_s is the Nyquist critical frequency). Indeed, during the statistically steady flow regime ($t \gtrsim 20$), the two solvers exhibit small-scale power that differ by more than one order of magnitude, with HLLD being in excess of 10^{-5} (at all resolutions) whereas HLL below 10^{-6}.

In terms of CPU time, computations carried out with HLLD (at medium resolution) were $\sim$1.9 slower than HLL.

4.2.3 *Axisymmetric jet propagation*

As a final example, we consider the propagation of a relativistic magnetized jet. For illustrative purposes, we restrict our attention to axisymmetric coordinates with $r \in [0, 20]$ and $z \in [0, 50]$. The jet initially fills the region $r, z \le 1$ with density $\rho_j = 1$ and longitudinal (z) velocity specified by $\gamma_j = 10$ ($v^r = v^\phi = 0$).

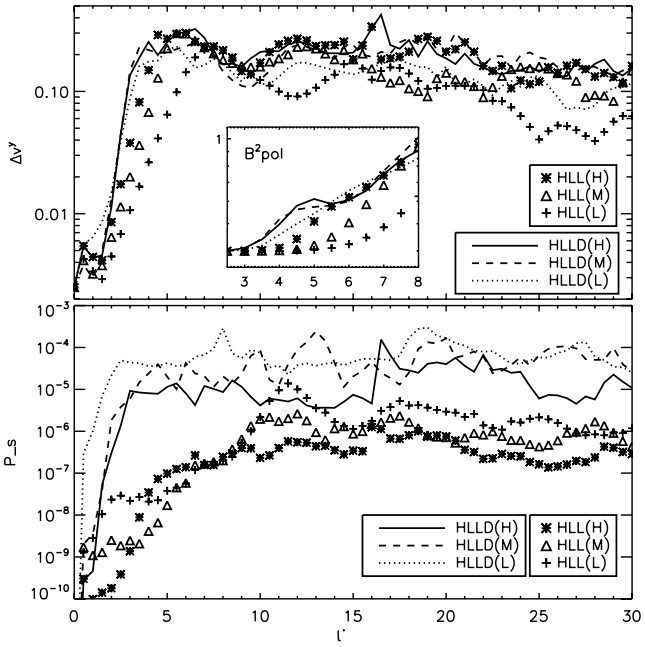

Figure 16. Top panel: growth rate (as a function of time) for the KH test problem computed as $\Delta v^y \equiv (v^y_{\max} - v^y_{\min})/2$ at low (L), medium (M) and high (H) resolutions. Solid, dashed and dotted lines show results pertaining to HLLD, whereas symbols to HLL. Bottom panel: small scale power as a function of time for the KH application test. Integrated power is given by $P_s = 1/2 \int_{k_s/2}^{k_s} \int_{-1}^{1} |V(k, y)|^2 \, \mathrm{d}y \, \mathrm{d}k$, where $v(k, y)$ is the complex, discrete Fourier transform of $v^y(x, y)$ taken along the x direction. Here, k_s is the Nyquist critical frequency.

The magnetic field topology is described by a constant poloidal term, B^z, threading both the jet and the ambient medium and by a toroidal component $B^\phi(r) = \gamma_j b_\phi(r)$ with

$$b_\phi(r) = \begin{cases} b_{\rm m} r/a & \text{for} \quad r < a, \\ b_{\rm m} a/r & \text{for} \quad a < r < 1, \end{cases} \tag{63}$$

where $a = 0.5$ is the magnetization radius and $b_{\rm m}$ is a constant and vanishes outside the nozzle. The thermal pressure distribution inside the jet is set by the radial momentum balance, $r\partial_{\rm r} p_{\rm g} = -b_\phi \partial_{\rm r}(r b_\phi)$ yielding

$$p_{\rm g}(r) = p_j + b_{\rm m}^2 \left[1 - \min\left(\frac{r^2}{a^2}, 1\right)\right], \tag{64}$$

where p_j is the jet/ambient pressure at $r = 1$ and recovered from the definition of the Mach number, $M = v_j \sqrt{\rho_j/(\Gamma p_j) + 1/(\Gamma - 1)}$, with $M = 6$ and $\Gamma = 5/3$, although we evolve the equations using the approximated Synge gas equation of state of Mignone & McKinney (2007).

The relative contribution of the two components is quantified by the two average magnetization parameters $\sigma_z \equiv B_z^2/(2\langle p_{\rm g}\rangle)$ $\sigma_\phi \equiv \langle b_\phi^2\rangle/(2\langle p_{\rm g}\rangle)$ yielding

$$b_{\rm m} = \sqrt{\frac{-4 p_j \sigma_\phi}{a^2(2\sigma_\phi - 1 + 4\log a)}}, \; B_z = \sqrt{\sigma_z \left(b_{\rm m}^2 a^2 + 2 p_j\right)}, \tag{65}$$

where for any quantity $q(r)$, $\langle q\rangle$ gives the average over the jet beam $r \in [0, 1]$. We choose $\sigma_\phi = 0.3$, $\sigma_z = 0.7$, thus corresponding to a jet close to equipartition.

The external environment is initially static ($\boldsymbol{v}_{\rm e} = 0$), heavier with density $\rho_{\rm e} = 10^3$ and threaded only by the constant longitudinal field B^z. Pressure is set everywhere to the constant value p_j.

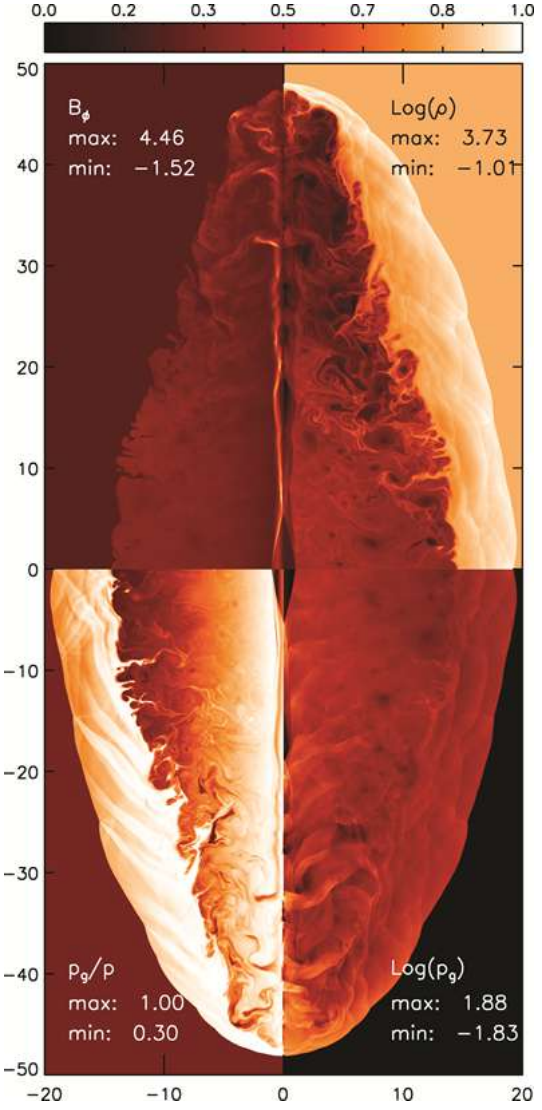

Figure 17. Left: composite colour map image of the jet at $t = 270$ at the resolution of 40 points per beam radius. In clockwise direction, starting from the top right-hand quadrant: density logarithm, gas pressure logarithm, thermal to total pressure ratio and ϕ component of magnetic field. The colour scale has been normalized such that the maximum and minimum values reported in each subplots correspond to 1 and 0.

We carry out computations at the resolutions of 10, 20 and 40 zones per beam radius ($r = 1$) and follow the evolution until $t = 300$. The snapshot in Fig. 17 shows the solution computed at $t = 300$ at the highest resolution.

The morphological structure is appreciably affected by the magnetic field topology and the ratio of the magnetic energy density to the rest mass, $b_\phi^2/\rho \approx 0.026$. The presence of a moderately larger poloidal component and a small Poynting flux favours the formation of a hammer-like structure rather than a nose cone (see Leismann et al. 2005; Mignone et al. 2005). At the termination point, located at $z \approx 40.5$, the beam strongly decelerates and expands radially promoting vortex emission at the head of the jet.

Close to the axis, the flow remains well collimated and undergoes a series of deceleration/acceleration events through a series of conical shocks, visible at $z \approx 4.5, 19, 24, 28, 32$. Behind these recollimation shocks, the beam strongly decelerates and magnetic

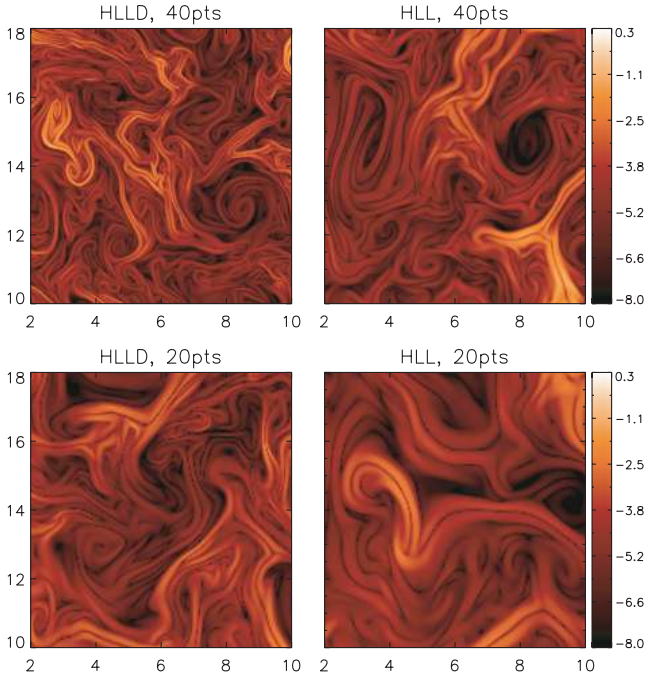

Figure 18. Enlargement of the turbulent flow region [2, 10] × [10, 18] at $t = 300$ showing the poloidal magnetic field structure (in log scale) for the high and medium resolution runs (40 and 20 points per beam radius).

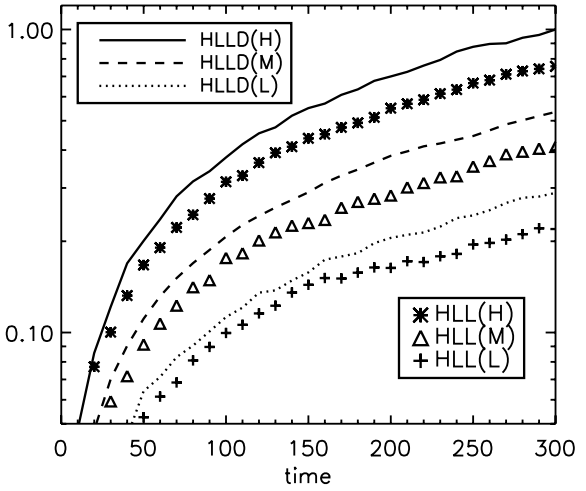

Figure 19. Volume average of $\nabla \boldsymbol{B}_{\rm p}^2/\boldsymbol{B}_{\rm p}^2$ as a function of time. Here, $\boldsymbol{B}_{\rm p}$ is the poloidal magnetic field. Solid, dashed and dotted lines refer to computations carried out with HLLD, whereas symbols give the corresponding results obtained with HLL.

tension promotes sideways deflection of shocked material into the cocoon.

The ratio $p_{\rm g}/p$ (bottom left-hand quadrant in Fig. 17) clearly marks the Kelvin–Helmholtz (KH) unstable slip surface separating the backflowing, magnetized beam material from the high-temperature (thermally dominated) shocked ambient medium. In the magnetically dominated region, turbulence dissipate magnetic energy down to smaller scales and mixing occurs. The structure of the contact discontinuity observed in the figures does not show suppression of KH instability. This is likely due to the larger growth of the toroidal field component over the poloidal one (Keppens et al. 2008). However, we also think that the small density ratio (10^{-3}) may favour the growth of instability and momentum transfer through entrainment of the external medium (Rossi et al. 2008).

For the sake of comparison, we also plot (Fig. 18) the magnitude of the poloidal magnetic field in the region $r \in [2, 10]$, $z \in [10, 18]$, where turbulent patterns have developed. At the resolution of 40 points per beam radius, HLLD discloses the finest level of small-scale structure, whereas HLL needs approximately twice the resolution to produce similar patterns. This behaviour is quantitatively expressed, in Fig. 19, by averaging the gradient of $\log(B_{\rm r}^2 + B_z^2)$ over the volume. Roughly speaking, HLL requires a resolution $\sim$1.5 that of HLLD to produce pattern with similar results.

5 CONCLUSIONS

A five-wave HLLD Riemann solver for the equations of relativistic magnetohydrodynamics has been presented. The solver approximates the structure of the Riemann fan by including fast shocks, rotational modes and the contact discontinuity in the solution. The gain in accuracy comes at the computational cost of solving a nonlinear scalar equation in the total pressure. As such, it better approximates Alfvén waves and we also found it to better capture slow shocks and compound waves. The performance of the new solver has been tested against selected one-dimensional problems, showing better accuracy and convergence properties than previously known schemes such as HLL or HLLC.

Applications to multidimensional problems have been presented as well. The selected tests disclose better resolution of small-scale structures together with reduced dependency on grid resolution. We argue that three-dimensional computations may actually benefit from the application of the proposed solver which, albeit more computationally intensive than HLL, still allows to recover comparable accuracy and resolution with a reduced number of grid zones. Indeed, since a relative change δ in the mesh spacing results in a factor of δ^4 in terms of CPU time, this may largely favour a more sophisticated solver over an approximated one. This issue, however, needs to receive more attention in forthcoming studies.

ACKNOWLEDGMENTS

The two- and three-dimensional computations reported in this paper were performed at CINECA in Bologna, Italy, thanks to INAF.

REFERENCES

Anile A. M., 1990, Relativistic Fluids and Magneto-fluids. Cambridge Univ. Press, Cambridge, p. 55
Anile M., Pennisi S., 1987, Ann. Inst. Henri Poincaré, 46, 127
Balsara D. S., 2001, ApJS, 132, 83
Berger M. J., Colella P. J., 1989, Comput. Phys., 82, 64
Brio M., WU C.-C., 1988, J. Comput. Phys., 75, 400
Bucciantini N., Del Zanna L., 2006, A&A, 454, 393
Davis S. F., 1988, SIAM J. Sci. Stat. Comput., 9, 445
Einfeldt B., Munz C. D., Roe P. L., Sjögreen B., 1991, J. Comput. Phys., 92, 273
Del Zanna L., Bucciantini N., Londrillo P., 2003, A&A, 400, 397 (dZBL)
Del Zanna L., Zanotti O., Bucciantini N., Londrillo P., 2007, A&A, 473, 11
Gammie C. F., McKinney J. C., Tóth G., 2003, A&J, 589, 444
Gehmeyr M., Cheng B., Mihalas D., 1997, Shock Waves, 7, 255
Giacomazzo B., Rezzolla L., 2006, J. Fluid Mech., 562, 223
Gurski K. F., 2004, SIAM J. Sci. Comput., 25, 2165
Harten A., Lax P. D., van Leer B., 1983, SIAM Rev., 25, 35
Honkkila V., Janhunen P., 2007, J. Comput. Phys., 223, 643
Keppens R., Meliani Z., van der Holst B., Casse F., 2008, A&A, 486, 663

Koldoba A. V., Kuznetsov O. A., Ustyugova G. V., 2002, MNRAS, 333, 932
Komissarov S. S., 1997, Phys. Lett. A, 232, 435
Komissarov S. S., 1999, MNRAS, 308, 1069
Leismann T., Antón L., Aloy M. A., Müller E., Martí J. M., Miralles J. A., Ibáñez J. M., 2005, A&A, 436, 503
Li S., 2005, J. Comput. Phys., 203, 344
Lichnerowicz A., 1967, Relativistic Hydrodynamics and Magnetohydrodynamics. Benjamin, New York
Mignone A., Bodo G., 2006, MNRAS, 368, 1040 (MB)
Mignone A., McKinney J. C., 2007, MNRAS, 378, 1118
Mignone A., Massaglia S., Bodo G., 2005, Space Sci. Rev., 121, 21
Mignone A., Bodo G., Massaglia S., Matsakos T., Tesileanu O., Zanni C., Ferrari A., 2007, ApJS, 170, 228
Miyoshi T., Kusano K., 2005, J. Comput. Phys., 208, 315 (MK)
Noh W. F., 1987, J. Comput. Phys., 72, 78
Press W., Teukolsky S., Vetterling W., Flannery B., 1992. Numerical Recipes in C, 2nd edn. Cambridge Univ. Press, Cambridge, UK
Romero R., Martí J. M., Pons J. A., Ibáñez J. M., Miralles J. A., 2005, J. Fluid Mech., 544, 323
Rossi P., Mignone A., Bodo G., Massaglia S., Ferrari A., 2008, A&A, 488, 795
Toro E. F., 1997, Riemann Solvers and Numerical Methods for Fluid Dynamics. Springer-Verlag, Berlin
Toro E. F., Spruce M., Speares W., 1994, Shock Waves, 4, 25
van der Holst B., Keppens R., Meliani Z., 2008, Comput. Phys. Commun., 179, 617

APPENDIX A: PROPAGATION OF ROTATIONAL DISCONTINUITIES

Left and right states across a rotational discontinuity can be found using the results outlined in Section 3.2. More specifically, we construct a family of solutions parametrized by the speed of the discontinuity K^x and one component of the tangential field on the right of the discontinuity. Our procedure can be shown to be equivalent to that of Komissarov (1997). Specifically, one starts by assigning $\rho, p_g, \boldsymbol{v}, \boldsymbol{B}^t$ on the left-hand side of the front [$\boldsymbol{B}^t \equiv (0, B^y, B^z)$] together with the speed of the front, K^x. Note that B^x cannot be freely assigned but must be determined consistently from equation (46). Expressing K^k ($k \neq x$) in terms of v^k, B^k and B^x and substituting back in the x component of equation (46), one finds that there are two possible values of B^x satisfying the quadratic equation:

$$a(B^x)^2 + bB^x + c = 0, \tag{A1}$$

where the coefficients of the parabola are

$$a = \eta - \frac{(\eta - K^x v^x)^2}{(K^x - v^x)^2}, \quad b = 2\chi \left(v^x + \frac{\eta - K^x v^x}{K^x - v^x} \right), \tag{A2}$$

and

$$c = w_g + \frac{\boldsymbol{B}^t \cdot \boldsymbol{B}^t}{\gamma^2} \tag{A3}$$

with $\eta = 1 - (v^y)^2 - (v^z)^2$, $\chi = v^y B^y + v^z B^z$ and γ being the Lorentz factor. The transverse components of $\boldsymbol{K}$ are computed as

$$K^{y,z} = v^{y,z} + \frac{B^{y,z}}{B^x}(K^x - v^x). \tag{A4}$$

On the right-hand side of the front, one has that ρ, p_g, w, B^x and $\boldsymbol{K}$ are the same, see Section 3.2. Since the transverse field is elliptically polarized (Komissarov 1997), there are, in principle, infinite many solutions and one has the freedom to specify, for instance, one component of the field (say B^y_R). The velocity $\boldsymbol{v}_R$ and the z component of the field can be determined in the following way. First, use equation (47) to express $v^k_{cL}(k = x, y, z)$ as a function of B^z_R for given B^x_R and B^y_R. Using the jump condition for the density together with the fact that ρ is invariant, we solve the non-linear equation:

$$\rho_L \gamma_L \left(K^x - v^x_L \right) = \rho_R \gamma_R \left(K^x - v^x_R \right), \tag{A5}$$

whose roots gives the desired value of B^z_R.

This paper has been typeset from a TEX/LATEX file prepared by the author.